

See discussions, stats, and author profiles for this publication at: <https://www.researchgate.net/publication/229106215>

Vapor deposited ethanol–H₂O ice mixtures investigated by micro–Raman scattering

ARTICLE in VIBRATIONAL SPECTROSCOPY · NOVEMBER 2006

Impact Factor: 2 · DOI: 10.1016/j.vibspec.2006.05.020

CITATIONS

10

READS

32

4 AUTHORS:



B. Chazallon

Université des Sciences et Technologies de ...

54 PUBLICATIONS 702 CITATIONS

SEE PROFILE



Yusuf Celik

Ruhr-Universität Bochum

15 PUBLICATIONS 62 CITATIONS

SEE PROFILE



Cristian Focsa

Université des Sciences et Technologies de ...

102 PUBLICATIONS 946 CITATIONS

SEE PROFILE



Yannick Guinet

Université des Sciences et Technologies de ...

86 PUBLICATIONS 1,175 CITATIONS

SEE PROFILE

Vapor deposited ethanol–H₂O ice mixtures investigated by micro-Raman scattering

Bertrand Chazallon^{a,*}, Yusuf Celik^a, Cristian Focsa^a, Yannick Guinet^b

^aLaboratoire de Physique des Lasers, Atomes et Molécules (PhLAM), Université Lille 1, UMR CNRS 8523, CERLA, 59655 Villeneuve d'Ascq, France

^bLaboratoire de Dynamique et Structure des Matériaux Moléculaires, Université Lille 1, UMR CNRS 8024, 59655 Villeneuve d'Ascq, France

Available online 24 July 2006

Abstract

Solid deposits have been formed at 88 K and 10^{−1} Torr from ethanol–water gas collected above aqueous solutions of ethanol (EtOH) (0.6, 2, 4.5, 9 and 17 mol%). The composition of different gas mixtures varying between 1:16 and 1:0.8 EtOH:H₂O are determined at 295 K using our experimental vapor–liquid equilibrium (VLE) data in combination with the Wilson model [28]. The Wilson constants derived at this temperature are $\Lambda_{12} = 0.37(4)$ and $\Lambda_{21} = 0.58(5)$. The concentration of EtOH in the ice mixture can be calculated using these data and a kinetic model of condensation. It is found to vary between 9 and 65 mol% EtOH. The ice mixtures are analyzed in situ in a modified cryostage by micro-Raman spectroscopy. The distinct vibrational signatures of pure EtOH, EtOH aqueous solutions and EtOH–ice mixtures are identified in the 400–3800 cm^{−1} spectral range. Internal vibrational motions of EtOH molecules are affected by temperature and concentration. The presence of amorphous EtOH–ice phases at 88 K is demonstrated by the characteristic vibrational signatures of the ν_{OH} stretching modes. The crystallization of an EtOH hydrate is proposed during annealing at ~ 140 K of a 65 mol% EtOH–ice mixture. According to our preliminary X-ray diffraction work, this phase has apparently a distinct structure from that of solid EtOH or from EtOH–clathrate structures usually found in frozen aqueous solutions. For ice mixtures of lower EtOH content, a distinct hydrate phase crystallizes at ~ 170 K. These results suggest that ice mixtures obtained by vapor deposition reflect the existence of EtOH clusters of a distinctive structural nature with respect to those encountered in frozen aqueous mixtures.

© 2006 Elsevier B.V. All rights reserved.

Keywords: Thin films; Vapor–liquid equilibrium; Ethanol; ice; Clathrate hydrates; Micro-Raman spectroscopy

1. Introduction

Ice represents one of the most prevalent condensed phases in the Earth's atmosphere and is particularly able to provide surfaces that can significantly interact with atmospheric trace gases. The gas–ice interaction may correspond to trapping processes that occur not exclusively in the atmosphere, but also in cold interstellar medium or comets at relatively lower temperature and pressure conditions. To date, an important number of studies have been performed on the interaction with ice of inorganic species like HCl or HNO₃, within the context and problematic of the formation of the ozone hole over Antarctica [1]. However, recent studies have shown that

light organics (alcohols, acetone, formaldehyde, etc.) can also play an important role in the upper troposphere [2] and snowpack chemistry [3]. Their evolution in the atmosphere can provide a substantial source of HO_x radicals that control photochemical cycles and ozone budget. In consequence, their interaction with ice can cause perturbation of this chemistry.

Principally two different ice growth mechanisms exist in the atmosphere: (1) gas–water co-condensation (or vapor depositional growth) and (2) collection of supercooled droplets by ice (riming) [4]. Rarely does either of these processes operate exclusively in clouds, however both contribute to the incorporation of gases that can affect the ice structure and modify the nature and composition of the incorporated species in ice, or in the gas phase. Our preliminary study on the effects of freezing on water–formaldehyde aqueous solutions at different concentrations confirms this assertion [5,6].

Studies carried out so far have mainly focused on the freezing process of aqueous solutions of ethanol (EtOH) in

* Corresponding author at: Laboratoire de Physique des Lasers, Atomes et Molécules, Université des Sciences et Technologies de Lille, 59655 Villeneuve d'Ascq Cedex, France. Tel.: +33 320336468; fax: +33 320336463.

E-mail address: chazallon@phlam.univ-lille1.fr (B. Chazallon).

relation with the phase diagram [7–12] and the determination of different stable or metastable EtOH hydrate structures by X-ray and differential scanning calorimetry (DSC) [9]. In this frame, the formation of clathrate hydrates has often been reported. In spite of the familiarity of alcohol–water systems and their importance in many fields of chemistry, cryobiology, astrophysics [13], there are still significant discrepancies in the literature with uncertainties concerning the composition and the structure of the stable or metastable eutectic or peritectic hydrates [9,11–12]. DSC experiments conducted recently [11] pointed out the relationship between the aqueous solution structure and the formation of metastable solid phases first separated from the supercooled liquid in the liquid–solid phase diagrams of many alcohol–water systems. Extensive X-ray studies [14,15] seem to corroborate this assertion as the structural transition of the predominant clusters from tetrahedral-like structure of water to hydrogen bonded alcohol chains is observed at ~ 0.17 mol fraction of EtOH in aqueous solutions. Moreover, the structure of dominant clusters formed in the liquid mixture is reflected into that of the frozen alcohol–water mixture. This view seems consistent with recent structural investigations performed on concentrated alcohol solutions that reveal the formation of hydrogen bonded clusters surrounded by water molecules bridging the neighboring alcohol clusters through hydrogen bonding [16].

On the other hand, a number of studies have been reported on the co-condensation of mixtures including water vapor and gas [17–20]. They mainly focused on structural information and on factors that determine the formation of clathrate hydrates. After deposition at temperature below 100 K of an appropriate water:guest vapor ratio, annealing in the 110–150 K range is required to promote crystallization of clathrates [19,20]. These ice-like solid compounds crystallize into distinct cubic structure (type I, with space group $Pm\bar{3}n$ and type II with space group $Fd\bar{3}m$) characterized by the presence of gas molecules (guests) stabilizing the host water structure [21]. Clathrate hydrates may also be involved in the efficient trapping of several gases by direct co-deposition at higher temperature ~ 200 K [22] with “polar” guests. Additionally, direct crystallization of the deposit may occur in the 100–150 K range if an appropriate amount of the occluded gas includes proton-acceptor molecules. It seems apparent that these latter convey greater orientational mobility of the water lattice at low temperature by creating mobile defects that facilitate the trapping of non (or weakly) polar gas molecules and ensure the crystallization of the deposit [23]. Ethanol represents an interesting case in that the molecule is suggested to form H-bonds with the water host lattice in samples prepared by freezing, which apparently leads to the formation a modified structure II or a metastable structure I [9,24]. Vapor deposited EtOH–ice mixtures may however behave differently with respect to frozen aqueous solutions. The slow dynamics of molecules at low temperature may inhibit the clustering process and induce some differences in the structural nature of the deposited products.

In the present study, preliminary results are reported on the characterization by micro-Raman scattering of EtOH-based

solid samples of different compositions formed by the co-condensation of EtOH–H₂O gas. Another issue emphasized in this contribution concerns the development of a temperature regulated reactor (from 77 to 400 K). It is specifically designed for in situ micro-Raman analysis and the synthesis at low pressure (down to 10^{-3} Torr, recently extended to 10^{-7} Torr) of thin ice films of 200–500 μm thickness. To monitor the structural effects of the EtOH concentration in the solid, the EtOH–H₂O gas composition is first determine from thermodynamic and condensation kinetics models before the deposition takes place. The effect of temperature is then analyzed by micro-Raman spectroscopy. To our knowledge, it is the first time that this system is investigated spectroscopically at low temperature ($77\text{ K} < T < 273\text{ K}$).

2. Experimental

2.1. Sample preparation

Pure EtOH purchased from Verbièse (France) (purity $> 99.77\%$) was mixed with double distilled and deionized water produced by an UHQ PS (Elgastat) (resistivity of $18\text{ M}\Omega\text{ cm}^{-1}$). Aqueous solutions of the following EtOH concentrations are prepared: 0.6, 2, 4.5, 9 and 17 mol%. Vapor–liquid equilibrium (VLE) of each EtOH aqueous solution is reached in a thermally insulated preparation chamber maintained at $295 \pm 1\text{ K}$ and separated from a FDCS 196 cryostage (Linkam) through an inline membrane valve. Originally designed for freeze-drying processes, the modified cryostage embodies significant improvements to ensure the alternative introduction of a closely controlled proportion of EtOH–water vapor mixtures or high purity nitrogen gas (Alphagaz class 2, 99.9999%). A schematic view of the experimental set-up used in the present experiment is given Fig. 1. Time is allowed for equilibrium before the condensation process starts. The downstream tubing from the preparation chamber and the cryostage is evacuated by a primary pump to a residual pressure of $\sim 10^{-3}$ Torr, reached at 88 K. During gas condensation, the total pressure in the cryostage is controlled continuously via a Pirani gauge while the pressure above the solutions is controlled with a SDX 15A₂ (Selectronic) (0–760 Torr) pressure gauge. This latter shows a remarkable reproducibility and was calibrated using a (0–1000 Torr) Ceramicel Varian absolute pressure gauge. The cryostage temperature is controlled with a precision of $\pm 0.1\text{ K}$. Dry nitrogen gas flow is used as refrigerant. When the vapor mixture is admitted in the pre-cooled cryostage (88 K) (Fig. 1), the pressure rapidly increases from 10^{-3} Torr up to a value adjusted manually at 10^{-1} Torr for all the set of experiments. The gas mixture is deposited on the cold element and an optimal Raman signal of the thin ice film is generally obtained after a 3–5 min deposit. The valve is subsequently closed and the pressure decreases down to the residual value in a few seconds. The temperature is then increased at a rate of 10 or 5 K/min, in 10 or 5 K increment steps. To avoid evaporation of the sample, high purity nitrogen gas is added at $\sim 120\text{ K}$, until the atmospheric pressure is reached.

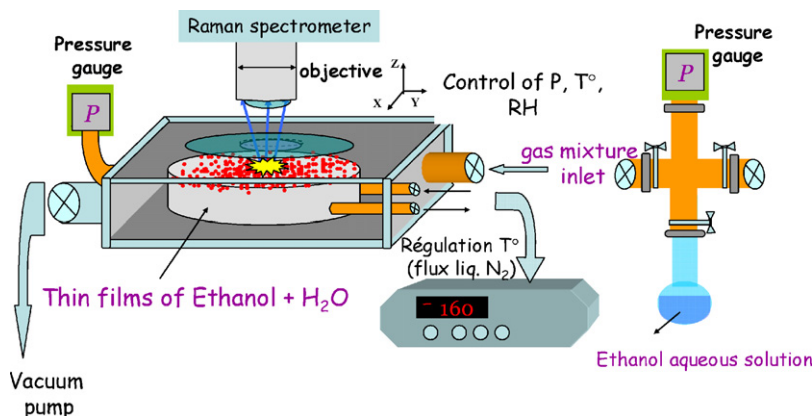


Fig. 1. Experimental set-up used for the measured equilibrium liquid–vapor of EtOH aqueous solutions and Raman analysis of vapor deposited EtOH–ice mixtures.

2.2. Micro-Raman

The Raman spectra are recorded using a XY-micro-Raman spectrometer (DILOR) equipped with an Olympus microscope (BX-40) on which the LINKAM stage is mounted. The excitation radiation ($\lambda = 514.5$ nm) is produced by an Ar laser source (Coherent). The scattered light is analyzed by using a triple dispersive spectrograph equipped with 1800 lines per mm gratings and a liquid–nitrogen-cooled CCD detector. A 200 μm entrance slit was typically used giving a 2 cm^{-1} mean spectral resolution. The laser power at the sample through the cell double windows (tri-silicate glass) is ~ 5 mW as measured with a Coherent FM power meter equipped with a LM 10 head. The circular beam spot size has a diameter of $\sim 2\text{ }\mu\text{m}$ when using a ULWD Olympus $50\times$ objective (0.6 numerical apertures – 7 mm working distance). The system works in a confocal configuration allowing nearly the total elimination of the contribution of the out-of-focus zones. The peak positions of the collected spectra were determined using a least square fitting procedure.

3. Results and discussion

3.1. Ice film composition

In the following, we carefully investigated the sample composition that represents a key parameter in the interpretation of our spectroscopic data. Formation of ice particles by co-condensation is known to be governed by a kinetics law [25] that determines the concentration of EtOH in the solid (X_{Eth}):

$$X_{\text{Eth}} = \left(1 + \frac{P_{\text{H}_2\text{O}} \alpha_{\text{H}_2\text{O}} \sqrt{M_{\text{Eth}}}}{P_{\text{Eth}} \alpha_{\text{Eth}} \sqrt{M_{\text{H}_2\text{O}}}} \right)^{-1}, \quad (1)$$

where P_i is the partial vapor pressure of a component i , α_i the mass accommodation coefficient (assumed to be 1 at 88 K), and M_i is the molar mass of the component i . This equation differs from earlier work [25], and was modified by us accordingly to account for the higher partial pressure of dopants chosen in our experiments.

According to this condensation mechanism, one may expect that the dopant concentration will be higher than its

thermodynamic solubility in ice such as in the case of HCl [25]. Moreover, the conditions of deposition (88 K, $P \sim 10^{-1}$ Torr) imply a high ice growth rate that corresponds to concentration values of X_{Eth} predicted by kinetics and relation (1) rather than the thermodynamics of the solid solution of the gas in ice. In contrast, a lower ice growth regime may lead to a significant change in the trapping efficiency of dopants and may correspond to a different structure and ice reactivity [26]. This emphasizes the importance to critically define the conditions of the sample preparation.

The ethanol/water vapor pressure ratio above the solutions is chosen to provide the desired concentration for the EtOH–ice mixtures. As we could find no experimental data for the vapor mixing ratio (EtOH:H₂O) at 295 K, we measure the actual VLE first at 303 K to validate our experimental protocol with existing literature data. Our values reported in Fig. 2 are found in good agreement with literature data obtained in similar conditions at 303 K [27]. We further perform VLE measurements at 295 K and derived estimates of the gas phase composition from the model developed by Wilson [28]. This model is proven to have a very high accuracy [27] for numerous

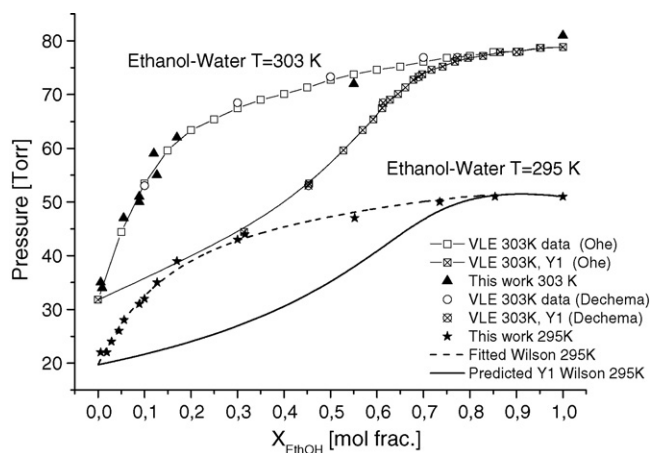


Fig. 2. Isothermal vapor–liquid equilibrium total pressure data as a function of ethanol–water mixture concentration. Literature data are compared with the present work for the 303 K isotherm. Measured gas phase compositions Y_1 are plotted as a function of EtOH concentration in the solution at 295 and 303 K. The Wilson isotherm is fitted to our experimental data at 295 K. The predicted isotherm Y_1 (295 K) curve is derived from the Wilson model (see text).

multi-component systems including binary alcohol–water systems. A brief summary of the model is described below.

When the ethanol–water vapor is in equilibrium with the binary liquid mixture, the fugacity of each component i in both phases is equal:

$$f_i^V = f_i^L, \quad (2)$$

where f_i is the fugacity, V and L correspond to the vapor and the liquid phase, respectively. If we assume that the gas phase follows an ideal gas law (which seems reasonable at least at low pressure), then $f_i^V = PY_i$ where P is the total pressure and Y_i is the mole fraction of the component i in the gas phase.

For a non-ideal solution like ethanol–water, the fugacity of the liquid phase is given by

$$f_i^L = P_i \gamma_i X_i \quad (3)$$

where γ_i is the activity coefficient and P_i is the vapor pressure of component i determined from the two parameter Clausius–Clapeyron equation: $\ln P_i = A_i - B_i/T$ with P_i in Torr and T in K. Tabulated values of A_i and B_i for EtOH are taken from Ref. [29]: $A_{\text{EtH}} = 23.16$ and $B_{\text{EtH}} = 5676$. On the other hand, for water, the Antoine equation is applied: $\ln P_i = A_i + B_i/(T + C_i)$ with P_i in Torr and T in K. The parameters are taken from the data of Ref. [30], with $A_{\text{H}_2\text{O}} = 18.3035$, $B_{\text{H}_2\text{O}} = -3816.44$ and $C_{\text{H}_2\text{O}} = -46.13$.

According to this model, the knowledge of the activity coefficient allows the determination of the gas phase composition, for a given dissolved EtOH concentration. The Wilson model thus expresses the degree of deviation of a non-ideal solution by the excess free energy ΔG^E , which is defined as $\Delta G^E = \Delta G - \Delta G^I$, i.e., the difference between the actual free energy (ΔG) and the free energy calculated in terms of the ideal solution (ΔG^I). Wilson obtains the following relation for this expression, based on the Flory–Huggins equation:

$$\frac{\Delta G^E}{RT} = - \sum_i X_i \ln \left[\sum_j X_j \Lambda_{ij} \right] \quad (4)$$

where R is the molar gas constant and Λ_{ij} are the Wilson constants. These latter describe the interaction between the molecules forming a solution. In contrast to other simplified models, the interaction depend on the probability of finding a molecular constituent i in the vicinity of a constituent j , and on the intermolecular interaction energy between the constituents. From this expression, Wilson derived the following relations for the activity coefficient of a binary mixture:

$$\ln(\gamma_1) = -\ln(X_1 + \Lambda_{12}X_2) + X_2 \left[\frac{\Lambda_{12}}{X_1 + \Lambda_{12}X_2} - \frac{\Lambda_{21}}{X_2 + \Lambda_{21}X_1} \right], \quad (5)$$

$$\ln(\gamma_2) = -\ln(X_2 + \Lambda_{21}X_1) - X_1 \left[\frac{\Lambda_{12}}{X_1 + \Lambda_{12}X_2} - \frac{\Lambda_{21}}{X_2 + \Lambda_{21}X_1} \right]. \quad (6)$$

Using (2), (3), (5) and (6), we derive the following Wilson constants from a least square fit of our experimental VLE

Table 1

Comparison between different ethanol–water mixture compositions

X_{EtOH} aqueous solutions (mol%)	Calculated Y_{EtOH} gas phase (mol%)	$P_{\text{EtOH}} : P_{\text{H}_2\text{O}}$ (gas phase)	Calculated condensed phase (X_{EtOH} mol%)
0.6 ^a	5.8	1:16	9 ^a
1	9.2	1:9.9	14
1.9 ^a	15.7	1:5.4	23 ^a
2.9	21.7	1:3.6	31
4.5 ^a	29.2	1:2.4	40 ^a
5.6	33.3	1:2.0	44
8.9 ^a	42.3	1:1.4	54 ^a
10	44.5	1:1.2	56
12.7	49	1:1.0	61
17 ^a	54.2	1:0.8	65 ^a

The equilibrium gas phase composition above the solutions is calculated from the Wilson model described in the text. The condensed phase composition is calculated according to the condensation model described in the text.

^a Sample analyzed by micro-Raman spectroscopy (this work).

data at 295 K: $\Lambda_{12} = 0.37(4)$ and $\Lambda_{21} = 0.58(5)$. With these parameters and (2), we calculate the gas phase composition as a function of P , the total pressure above the solution, for the isotherm at 295 K (see Fig. 2). Fig. 2 also displays the VLE isotherm at 303 K including both experimental data (from Ref. [27] and the present work) and gas phase calculations according to the Wilson model. Both results match in detail, giving us a good confidence for the prediction made at 295 K. Using Eq. (1), and the predicted gas phase composition, we calculate the actual solid phase composition of the ice film deposited at 88 K. These results are summarized in Table 1.

3.2. Raman spectra

3.2.1. EtOH aqueous solutions

We first briefly examine the situation in the liquid in order to get characteristic spectral references before considering the situation in the vapor deposited solid mixtures. Fig. 3 displays Raman spectra of EtOH aqueous solutions at 0.6, 2, 4.5, 9 and 17 mol% EtOH and pure liquid EtOH, collected at ambient temperatures in the 2710–3785 cm^{-1} spectral range. Experimentally observed frequencies of pure EtOH and the 4.5 mol% EtOH solution are reported in Table 2, along with the assignments of the different bands observed. The bands at ~ 2889 , ~ 2938 and $\sim 2986 \text{ cm}^{-1}$ assigned to the different C–H stretching modes of the EtOH molecules are plotted as a function of X_{EtH} in Fig. 4A. They show a characteristic decrease in frequency as X_{EtH} increases. The softening of the C–H bonds is explained by a partial and gradual electron transfer from the hydrogens and carbon to the oxygen of the EtOH molecule. This view is consistent with the gradual increase with concentration of the H-bond strengths of the EtOH molecules [31]. This also highlights the role played by the EtOH oxygen acceptor or the end chain EtOH proton donor in H-bonds formation. The effect is apparently equally pronounced for the CH_3 and CH_2 hydrogens, thus indicating a complete participation of all hydrogens.

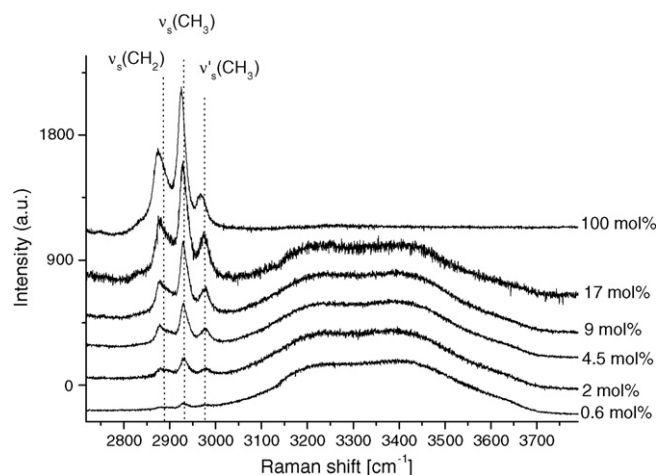


Fig. 3. Raman spectra of aqueous solutions containing variable amounts of EtOH at room temperature. The spectra cover the frequency range 2720–3790 cm^{-1} . Vertical dotted lines indicate the band position and the corresponding C–H modes of the 0.6 mol% in order to highlight the effect of EtOH concentration.

In the C–O vibrational spectral region, we observe that the band frequencies at ~ 879 and $\sim 1045 \text{ cm}^{-1}$ corresponding to $\nu_s(\text{CCO})$ and $\nu_a(\text{CCO})$ stretching modes versus X_{EtOH} present a blue shift as the concentration increases (Fig. 4B). This is attributed to an increasing covalency of the C–O bond, which is consistent with the partial transfer of electrons from CH_3 carbon of EtOH to the end chain oxygen and the polarisation of the O–H bond in accordance with previous NMR and infrared studies [31]. This illustrates an increase in the H-bond strengths as described above in the case of the C–H stretching. The situation remains similar for the band at $\sim 1086 \text{ cm}^{-1}$ ascribed to mixed modes involving the contribution of $\delta(\text{COH})$. Although these results need to be confirmed at higher concentration, they globally follow the trend observed by infrared spectroscopy. Hence, they support the hypothesis of a clathrate-like structure of water in the water-rich region, in which small hydrogen bonded EtOH clusters are surrounded by H-bonded water molecules increasing the strength of their H-bonds as the EtOH concentration increases. In agreement with

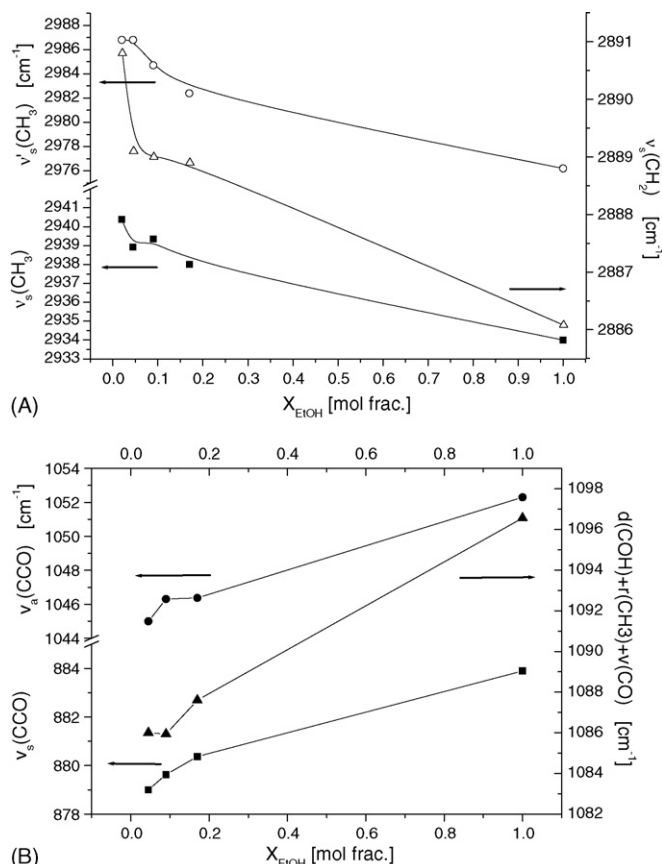


Fig. 4. (A) Evolution of the frequency of the different C–H stretching modes as a function of EtOH concentration in the solution. Frequency corresponding to the $\nu_s(\text{CH}_2)$ mode of the 0.6 mol% may be affected by a great uncertainty due to the low signal to noise ratio. (B) Evolution of the frequency of the different C–O stretching modes as a function of EtOH concentration in the solution. The band positions of the 0.6 mol% have been omitted due to the low signal to noise ratio obtained and the difficulty to extract meaningful data.

previous infrared work, the rate of change of the H-bond strength seems to vary continuously (with no discontinuity) with increasing EtOH concentration (Fig. 4A and B). This suggests that H-bond formation between water molecules and EtOH is unfavourable at least in the water rich part. On the other

Table 2
Wavenumbers and assignments of the Raman bands in different Ethanol-based compounds

EtOH pure liquid (295 K)		4.5 mol% EtOH aqueous solution (295 K)		40 mol% EtOH—ice mixtures 88 K		40 mol% EtOH—ice mixtures 188 K	
$\nu \text{ (cm}^{-1}\text{)}$	Assignment	$\nu \text{ (cm}^{-1}\text{)}$	Assignment	$\nu \text{ (cm}^{-1}\text{)}$	Assignment	$\nu \text{ (cm}^{-1}\text{)}$	Assignment
433	$\delta(\text{CCO})$	439	$\delta(\text{CCO})$	440	$\delta(\text{CCO})$	—	$\delta(\text{CCO})$
884	$\nu_s(\text{CCO})$	879	$\nu_s(\text{CCO})$	881	$\nu_s(\text{CCO})$	883	$\nu_s(\text{CCO})$
1052	$\nu_a(\text{CCO})$	1045	$\nu_a(\text{CCO})$	1050	$\nu_a(\text{CCO})$	1052	$\nu_a(\text{CCO})$
1096.5	$\nu(\text{CO}) + \nu(\text{CH}_3) + \delta(\text{COH})$	1086.5	$\nu(\text{CO}) + \nu(\text{CH}_3) + \delta(\text{COH})$	1090	$\nu(\text{CO}) + \nu(\text{CH}_3) + \delta(\text{COH})$	1091	$\nu(\text{CO}) + \nu(\text{CH}_3) + \delta(\text{COH})$
1278	$\nu(\text{CH}_2) + \delta(\text{COH})$	1277.6	$\nu(\text{CH}_2) + \delta(\text{COH})$	1278	$\nu(\text{CH}_2) + \delta(\text{COH})$	1277	$\nu(\text{CH}_2) + \delta(\text{COH})$
1386	$\delta_s(\text{CH}_3)$	—	$\delta_s(\text{CH}_3)$	1382.5	$\delta_s(\text{CH}_3)$	—	$\delta_s(\text{CH}_3)$
1452.7	$\delta'_s(\text{CH}_3)$	1453.5	$\delta'_s(\text{CH}_3)$	1454.3	$\delta'_s(\text{CH}_3)$	1453	$\delta'_s(\text{CH}_3)$
1482	$\delta(\text{CH}_2)$	—	$\delta(\text{CH}_2)$	1486.3	$\delta(\text{CH}_2)$	1484	$\delta(\text{CH}_2)$
2886	$\nu_s(\text{CH}_2)$	2889	$\nu_s(\text{CH}_2)$	2888.6	$\nu_s(\text{CH}_2)$	2886	$\nu_s(\text{CH}_2)$
2934	$\nu_s(\text{CH}_3)$	2938	$\nu_s(\text{CH}_3)$	2937	$\nu_s(\text{CH}_3)$	2935	$\nu_s(\text{CH}_3)$
2976	$\nu'_s(\text{CH}_3)$	2986	$\nu'_s(\text{CH}_3)$	2983	$\nu'_s(\text{CH}_3)$	2981	$\nu'_s(\text{CH}_3)$

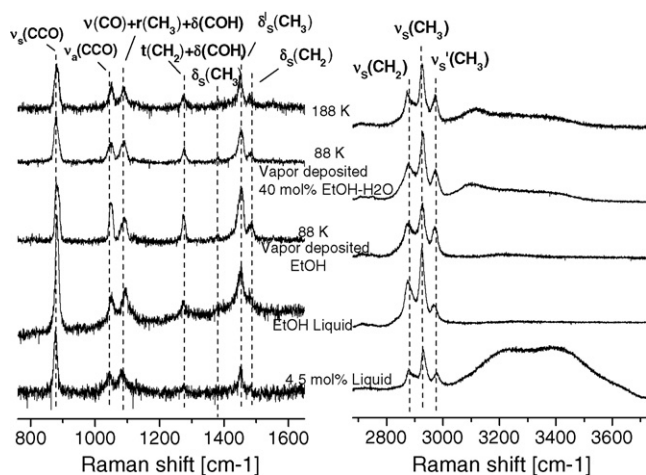


Fig. 5. Raman spectra recorded in different spectral regions (810–1530 cm^{-1} and 2670–3730 cm^{-1}) of liquid and vapor deposited pure EtOH and EtOH–water mixtures. The dotted vertical lines indicate the band positions and corresponding modes in the liquids. Raman spectra of the deposited mixtures collected at different temperatures are also indicated. Note the differences in the positions and bandwidths for the C–C–O modes (see text).

hand, in solutions with high EtOH content, Matsumoto et al. [32] proposed the formation of polymer hydrates in which most water molecules are not bonded to each other, but exist just as stabilizer of the EtOH large clusters (5–15 EtOH molecules).

3.2.2. Vapor deposited EtOH/H₂O mixtures

Fig. 5 displays a comparison of spectra recorded in different spectral regions (770–1530 cm^{-1} and 2670–3730 cm^{-1}) of liquid and vapor deposited pure EtOH and EtOH–water mixtures. The experimental frequencies of the vapor deposited 40 mol% EtOH–H₂O mixture at 88 and 188 K are listed in Table 2. The assignments are based on the previous infrared extensive work of Perchard and Josien [33] of liquid and solid EtOH. We will focus here on the characteristic spectral changes observed between the different spectra presented in Fig. 5. A detailed discussion of the temperature evolution of the C–O and C–H vibrational spectral regions will be presented in a separate contribution. One may be surprised by the fact that no dramatic changes occur and that only subtle differences exist between the spectra of the liquid and those of the solid mixtures in both spectral regions. For instance, a comparison between the liquid and the amorphous mixtures (at 88 K) reveals that the band ascribed to $\nu_s(\text{CCO})$ at $\sim 879 \text{ cm}^{-1}$ in the 4.5 mol% solution is increased almost linearly by ~ 2 and 5 cm^{-1} in the 40 mol% EtOH and pure EtOH deposits respectively. Similarly the band at $\sim 1045 \text{ cm}^{-1}$ assigned to $\nu_a(\text{CCO})$ is blue-shifted (almost linearly) by ~ 5 and 7 cm^{-1} in the 40 mol% EtOH and pure EtOH deposits, respectively. As discussed above in the case of the liquid mixtures, this effect may reflect the increasing concentration of EtOH in the deposited mixtures. One should note that the $\nu(\text{CCO})$ positions are not significantly affected when changing from liquid to the amorphous pure EtOH at 88 K. On the other hand, the bandwidth seems more sensitive to the liquid–amorphous solid conversion as displayed in Fig. 5. In passing from the liquid to the amorphous state, the bandwidth

of the band assigned to $\nu_s(\text{CCO})$ increases by ~ 2 and $\sim 6 \text{ cm}^{-1}$ for the EtOH mixtures and pure EtOH, respectively. In contrast, the effect of temperature (at 88 and 188 K) and the expected presence of a crystalline state (see next paragraph) for the 40 mol% EtOH mixture can not be straightforwardly seen on Fig. 5. A comparison with the liquid phase (4.5 mol% EtOH) indicates that the bands ascribed to $\nu_s(\text{CCO})$ and $\nu_a(\text{CCO})$ at 188 K are blue-shifted by ~ 4 and 7 cm^{-1} respectively, i.e. slightly more than at 88 K. It is thus tempting to attribute this larger shift to the crystallization of the mixture. However, the change in temperature may also be responsible for the observed shift, and the extent and relative magnitude of both effects cannot be discussed only based on these data alone. One may thus refer to the discussion presented in the next section.

3.2.3. O–H vibrational mode spectral region

In EtOH solutions, since the water is the solvent, the intensity of the bands at ~ 3260 and $\sim 3400 \text{ cm}^{-1}$ corresponding to O–H stretching modes reflects mainly the contribution from water molecules. Moreover, the symmetric and antisymmetric O–H modes are both sensitive to intermolecular interactions. The overlap with the band corresponding to O–H stretching of EtOH (weak and broad band at $\sim 3270 \text{ cm}^{-1}$ in pure EtOH) does not allow a clear distinction of the different molecular contributions. The isotopic dilution method is certainly the best way to discriminate between the O–H group frequencies.

However, in the condensed ice mixtures, the bands corresponding to the O–H modes are shifted to lower frequencies and transformed into a band of asymmetric shape. The most intense part of this band with symmetric shape is known to correspond predominantly to ν_{OH} symmetric stretching in ice. Therefore, any changes in the inter- or intramolecular interactions may induce observable variations on this well resolved band. In the following, we examine the temperature evolution of this band for the different ice mixtures.

3.2.3.1. The 88–160 K range. The evolution of ν_{OH} for pure ice and EtOH–ice mixtures is plotted as a function of the temperature on Fig. 6A and B. ν_{OH} in pure ice increases with temperature, in agreement with previous investigations [34,35]. This is generally attributed to a volume increase with temperature and partially reflects the decreasing strength of the H-bonds as temperature increases. As noted earlier [36] other coupled effects such as a strong intermolecular coupling, anharmonicity of the bonded water molecules or the specific local H-bond geometry may also account for the frequency shift with temperature. Pure amorphous ice (as) shows a striking difference with the crystalline hexagonal ice (Ih) in the band positions: for example at 100 K, the band frequency difference is $(\nu_{\text{OH}}^{\text{as}} - \nu_{\text{OH}}^{\text{Ih}}) \sim 22 \text{ cm}^{-1}$. This known effect reflects the distinct local structure and bonding of the metastable amorphous ice phase, with the presence of weaker H-bonds compared to the crystalline state. Note that our Raman spectrum of cubic ice and hexagonal ice did not show significant differences. In agreement with earlier studies, we will assume that the band shifts observed in the range 140 to $\sim 150 \text{ K}$ correspond to the transition from amorphous to cubic ice [37].

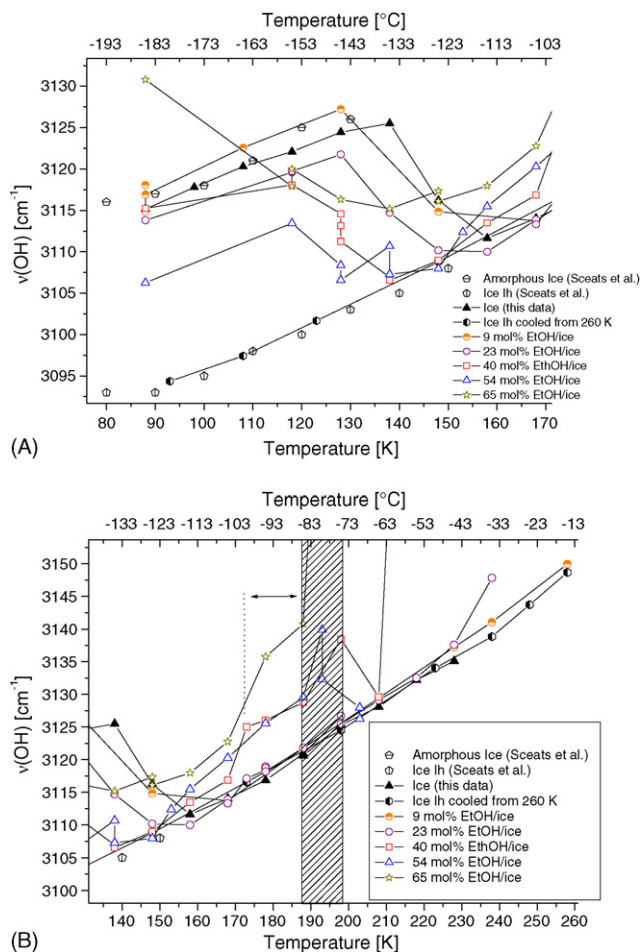


Fig. 6. (A) Temperature evolution between 80 and 170 K of the ν_{OH} symmetric stretching of pure ice and vapor deposited ice mixtures with various EtOH concentration (see symbols in the text box legend). Literature data for pure ice are given for comparison. Note the decrease of $\nu_{\text{OH}}^{\text{mixt}}$ with temperature compared to that of ν_{OH} for pure ice (see discussion). (B) Similar plot in another temperature range (130–260 K) (see symbols in the text box legend). The vertical hatched bands indicate the approximate temperature of the hydrate dissociation. The vertical dotted lines and horizontal arrow indicate the temperature of formation of a distinct hydrate for the 40 and 54 mol% EtOH-ice mixtures (see discussion).

A remarkable feature displayed in Fig. 6A is the evolution with temperature of the different mixtures between 88 and 160 K. At 88 K, all mixtures are apparently amorphous, as suggested by the band positions close to $\nu_{\text{OH}}^{\text{as}}$ or higher than $\nu_{\text{OH}}^{\text{Ih}}$. This corresponds to a less hydrogen bonded O–H stretching state compared to ice Ih. $\nu_{\text{OH}}^{\text{mixt}}$ is found to decrease rapidly with temperature compared to pure amorphous ice. It is associated with the onset of crystallization of the mixtures and suggests the appearance of ice Ic. The rate of conversion to a crystalline state seems thus enhanced by the increased of EtOH content. $\nu_{\text{OH}}^{\text{mixt}}$ reaches earlier the virtual linear boundary limit of $\nu_{\text{OH}}^{\text{X-tal-ice}}$ (pure crystalline ice) compared with pure ice (in the ~130–150 K range for the 23 mol% EtOH-ice and in the ~120–140 K range for the 40 and 54 mol% EtOH-ice, Fig. 6A). Ethanol seems thus to act as a catalyst in the conversion of amorphous ice to crystalline ice.

In contrast, the 65 mol% sample never reaches the lower virtual limit of $\nu_{\text{OH}}^{\text{X-tal-ice}}$ attributed to the onset of Ic crystallization. This may indicate that the amorphous mixture do not transform in Ic, but rather in a crystalline hydrate structure of ethanol between ~130 and ~140 K. It is composed of H-bonds weaker than those found in the crystalline ice structure. We attribute the temperature corresponding to the onset of crystallization to a minimum in the profile of the 65 mol% sample defined by $\nu_{\text{OH}}^{\text{mixt}}$ on Fig. 6A. Our preliminary X-ray diffraction work performed in similar experimental conditions [38] corroborates this conclusion. Further Raman and X-ray diffraction studies are in progress to refine the structure found for this hydrate. Although improbable in our case, one should stress however that phase separation (with the formation of a crystalline phase of pure ethanol embedded in non crystalline ice) as observed in hyper-quenched THF–water mixtures [39] cannot be completely ruled out. However, this situation seems to us unrealistic because the local hydrogen bonded structure of water is expected to relax first toward crystalline ice Ic considering the loss of molecular mobility of EtOH below the fictive temperature of water. The crystallization of ice Ic would thus have first driven the EtOH out of the crystal as it is the case for THF–water mixture. Moreover, a high EtOH concentration seems not especially required to promote this hydrate formation [38].

The difference ($\nu_{\text{OH}}^{\text{mixt}} - \nu_{\text{OH}}^{\text{X-tal-ice}}$) of $\sim 7 \text{ cm}^{-1}$ at 150 K is not inconsistent with the formation of a clathrate. A comparable value ($\sim 4 \text{ cm}^{-1}$) was previously reported for THF–structure II (tetrahydrofuran) [40] at somewhat higher temperature (255 K) and was partially attributed to the distorted H-bond geometry and the distribution of the intermolecular distances occurring in clathrates. However, our preliminary X-ray results do not corroborate the formation of either structure I or II. We believe that this new ethanol hydrate phase, which seems very stable over the temperature range investigated, may have a different structural nature with respect to the crystalline clathrate phases obtained at higher temperature (between ~150 and ~200 K) [9,12] in frozen aqueous solutions. This may be caused by the different nature of clusters formed in the vapor phase or during the condensation at low temperature. Additionally, the slow dynamics of deposited molecules at low temperature may inhibit clustering processes such as those observed in frozen samples.

3.2.3.2. Crystallization between 160 and 210 K. $\nu_{\text{OH}}^{\text{mixt}}$ exhibits a continuous drift to higher frequencies with respect to $\nu_{\text{OH}}^{\text{X-tal-ice}}$ as temperature increases. This effect happens already at ~155 K for the 40 and the 54 mol% EtOH-ice mixtures (Fig. 6B). It may correspond to the formation of the ethanol hydrate that coexists with small quantities of ice Ic formed at lower temperature. Furthermore, the rate of change of $\nu_{\text{OH}}^{\text{mixt}}$ with temperature reaches a “plateau” (constant slope, Fig. 6B) at ~170 K which is prolonged until ~188 K. Such changes and non-linear effects in the OH band displacement are consistent with a structural rearrangement in the crystal. It is thus conceivable that a different ethanol hydrate is formed at ~170 K. Such structural changes may induce the formation of H-bonds between EtOH and water molecules having a different

nature with respect to ice. On the other hand, a distorted water lattice and the existence of a distribution of OH...O distances due to the formation of an ethanol clathrate will cause variations in the H-bonds' strength and, thus, of $\nu_{\text{OH}}^{\text{mixt}}$. It is therefore tempting to attribute the observed band shift to the formation of a clathrate structure. This is also supported by the fact that the crystallization temperature (~ 170 K) falls in the range of stability and coexistence of clathrate hydrates according to the phase diagram of frozen EtOH aqueous solutions [9]. However, on the basis of this preliminary report alone, it is at evidence difficult to safely establish the exact structure.

Above ~ 188 K, the frequency of the band assigned to $\nu_{\text{OH}}^{\text{mixt}}$ dramatically increases for mixtures of EtOH content higher than 23 mol%. This is explained by the incongruent melting of the solid mixtures. Only ice Ih and a viscous liquid presumably composed of ethanol remains after melting of the hydrate. A next step in temperature leads to the melting of the complete samples between ~ 208 and 218 K for 40 mol%, at ~ 213 K for 54 mol%. Presence of ice Ih after melting of the hydrate is not detected in the 65 mol% sample. The melting of the 9 and 23 mol% samples is hardly detectable using this spectral region.

4. Conclusion

Micro-Raman spectroscopy proves to be a very sensitive probe to investigate thin doped ice films produced by vapor deposition. This is realized in a dedicated cryostage developed for low temperature and low pressure applications. Our experimental VLE data are used in combination with the Wilson model and a kinetic model of condensation to determine the composition of the different gas mixtures before and after deposition. In agreement with previous investigations, the Raman analysis performed on EtOH aqueous solutions suggests the existence of H-bonded EtOH clusters in which the H-bond strength is found to increase with EtOH concentration. Previous X-ray diffraction works [14,15] have suggested that the structure of the dominant clusters formed in the liquid mixture is reflected into that of the frozen alcohol–water mixture. In contrast, this preliminary Raman study of vapor deposited EtOH–ice mixtures suggests significant differences with respect to frozen aqueous solutions. The presence of amorphous EtOH–ice mixtures at 88 K is demonstrated by the characteristic vibrational signatures of the symmetric O–H stretching that shows close resemblance with that of pure amorphous ice. Depending on the gas phase composition, different crystalline phases can be formed during the annealing process. The crystallization of an EtOH hydrate is proposed at ~ 140 K for EtOH–ice mixture of 65 mol%, i.e. at a temperature slightly lower than the amorphous to cubic transition in pure ice. For ice mixtures of lower EtOH content, a distinct hydrate phase crystallizes at ~ 170 K, in the domain of existence of clathrate phases according to the EtOH–water phase diagram. Moreover, cubic ice (Ic) does not systematically appear, depending on the incorporated amount of EtOH in the ice mixtures. These results suggest that solid ice mixtures obtained by vapor deposition reflects the presence of EtOH clusters of a

distinctive structural nature with respect to those encountered in frozen aqueous mixtures. One can anticipate that long chains polymers are likely to behave similarly and that the extent of such effects may be enhanced at high concentration. Our recent Raman studies suggest that formaldehyde, an important volatile organic compound in the atmosphere, behaves similarly [41]. In the next step, the production of vapor deposited samples will be extended to lower pressure (down to 10^{-7} Torr) in order to closely reflect the natural conditions of ice formation in the atmosphere.

Acknowledgments

The Centre d'Etudes et de Recherches Lasers et Applications is supported by the Ministère Chargé de la Recherche, the Région Nord – Pas de Calais and the Fonds Européen de Développement Economique des Régions. This research is partially supported by the “Programme National de Chimie Atmosphérique” (PNCA) of the Centre National de la Recherche Scientifique (CNRS).

References

- [1] S. Solomon, *Rev. Geophys.* 37 (1999) 275.
- [2] H. Singh, Y. Chen, A. Staudt, D. Jacob, D. Blake, B. Heikes, J. Snow, *Nature* 410 (2001) 1078.
- [3] F. Dominé, P.B. Shepson, *Science* 297 (2002) 1506.
- [4] H.R. Pruppacher, J.D. Klett, *Microphysics of Clouds and Precipitation*, Reidel, Dordrecht, 1978.
- [5] B. Chazallon, N. Lebrun, P. Dhamelincourt, C. Toubin, C. Focsa, *J. Phys. Chem. B* 109 (2005) 432.
- [6] C. Mihsan, N. Lebrun, M. Ziskind, B. Chazallon, C. Focsa, J.L. Destombes, *Surf. Sci.* 566–568 (2004) 650.
- [7] G. Vuillard, N. Satragno, *C. R. Acad. Sci.* 260 (1960) 3841.
- [8] A.D. Pott, D.W. Davidson, *J. Phys. Chem.* 69 (1965) 996.
- [9] P. Boutron, A. Kaufmann, *J. Chem. Phys.* 68 (1978) 5032.
- [10] J.B. Ott, J.R. Goates, B.A. Waite, *J. Chem. Thermodyn.* 11 (1979) 739.
- [11] K. Takaizumi, T. Wakabayashi, *J. Solution Chem.* 26 (1997) 927.
- [12] S.S.N. Muthy, *J. Phys. Chem. A* 103 (1999) 7927.
- [13] F. Franks, J. Desnoyers, Alcohol–water mixtures revisited, in: F. Franks (Ed.), *Water Science Reviews*, vol. 1, Cambridge University Press, Cambridge, 1985, pp. 171–227.
- [14] N. Nishi, S. Takahashi, M. Matsumoto, A. Tanaka, K. Muraya, T. Takamuku, T. Yamaguchi, *J. Phys. Chem.* 99 (1995) 462.
- [15] T. Takamuku, K. Saisho, S. Nozawa, T. Yamaguchi, *J. Mol. Liq.* 119 (2005) 133.
- [16] S. Dixit, J. Crain, W.C. Poon, J.L. Finney, A.K. Soper, *Nature* 416 (2002) 829.
- [17] K. Consani, G.C. Pimentel, *J. Phys. Chem.* 91 (1987) 289.
- [18] J.E. Bertie, J.P. Devlin, *J. Chem. Phys.* 78 (10) (1983) 6340.
- [19] F. Fleyfel, J.P. Devlin, *J. Phys. Chem.* 92 (1988) 631.
- [20] H.H. Richardson, P.J. Wooldridge, J.P. Devlin, *J. Chem. Phys.* 83 (1985) 4387.
- [21] M. von Stackelberg, *Naturwissenschaften* 36 (1949) 327, and 359.
- [22] R.J. Fezza, J.M. Calo, *Geophys. Monogr. Am. Geophys. Union* 26 (1982) 157.
- [23] D.W. Davidson, J.A. Ripmeester, in: J.L. Atwood, J.E.D. Davies, D.D. MacNicol (Eds.), *Inclusion Compounds*, vol. 3, Academic Press, San Diego, CA, 1984, p. 69.
- [24] L.D. Calvert, P. Srivastava, *Acta Cryst. Sect. A* 25 (1969) S131.
- [25] F. Dominé, E. Thibert, *Geophys. Res. Lett.* 23 (24) (1996) 3627.
- [26] F. Dominé, C. Rauzy, *Atmos. Chem. Phys. Discuss.* 4 (2004) 4719.

- [27] J. Gmehling, U. Onken, J.R. Rarey-Nies, Liquid Equilibrium Data Collection, Dechema Chemistry Data Series, vol. I/2e, Dechema, Frankfurt, 1977.
- [28] G. Wilson, J. Am. Chem. Soc. 86 (1964) 127.
- [29] V. Devarakonda, A.K. Ray, J. Colloid Interface Sci. 221 (2000) 104.
- [30] M. Albert, I. Hahnenstein, H. Hasse, G. Maurer, AIChE J. 42 (1996) 1741.
- [31] K. Mizuno, Y. Miyashita, Y. Shindo, H. Ogawa, J. Phys. Chem. 99 (1995) 3225.
- [32] M. Matsumoto, N. Nishi, T. Furusawa, M. Saita, T. Takamuku, M. Yamagami, T. Yamaguchi, Bull. Chem. Soc. Jpn. 68 (1995) 1775.
- [33] J.-P. Perchard, M.-L. Josien, J. Chim. Phys. Chim. Biol. 65 (1969) 1856.
- [34] T.C. Sivakumar, S.A. Rice, M.G. Sceats, J. Chem. Phys. 69 (1978) 3468.
- [35] P.T.T. Wong, E. Whalley, J. Chem. Phys. 62 (1975) 2418.
- [36] G.P. Johari, H.A.M. Chew, Phil. Mag. B 49 (1984) 647.
- [37] V.F. Petrenko, R.W. Whitworth, Physics of Ice, Oxford University Press, 1999.
- [38] B. Chazallon, et al., in preparation.
- [39] C.A. Tulk, Y. Ba, D.D. Klug, G. McLaurin, J.A. Ripmeester, J. Chem. Phys. 110 (1999) 6475.
- [40] G.P. Johari, G.P. Chew, Nature 303 (1983) 604.
- [41] B. Chazallon, C. Focsa, C. Toubin, Y. Guinet, in preparation.